

Small Scale Models Subjected to Buried Blast Loading Part I: Floorboard Accelerations and Related Passenger Injury Metrics with Protective Hulls

Xing Zhao · Gary Shultis · Ryan Hurley ·
Michael Sutton · William Fourney · Uli Leiste ·
Xiaomin Deng

Received: 1 November 2012 / Accepted: 19 November 2013 / Published online: 5 December 2013
© Society for Experimental Mechanics 2013

Abstract Small scale models representing key vehicle structural elements, including both floorboards and bottom-mounted, downward V-shape hulls in various configurations, have been manufactured and subjected to a range of buried blast loading conditions. By varying surface stand-off distance and depth of burial for several hull and structure configurations, the *input-scaled response* of aluminum full-scale vehicle floorboards has been quantified using high speed stereo-vision. Specifically, the maximum vertical acceleration on the floorboard and the corresponding Head Injury Criterion (HIC_{15}) are quantified as metrics to assess the severity of the blast event. Results show standard V-shaped hulls provide essential blast mitigation, with reductions in floorboard measurements up to 47X in maximum acceleration and HIC_{15} . Though variations in protective hull geometry provide modest reductions in the severity of a floorboard blast event, results also show that personnel on typical floorboard structures during blast loading events will incur unacceptable shock loading conditions, resulting in either serious or fatal injury. A more appropriate design scenario would be to consider situations that employ frame-mounted passenger seating to reduce the potential for injury. A second set of experiments

will be presented in Part II that focuses on frame motions and accelerations when steel frames and steel structures are employed with various frame connections and coatings for frame blast mitigation.

Keywords Blast mitigation · Hull designs · Small scale model · Head injury criteria · Acceleration measurements · Stereo-vision

Introduction

The adverse physiological consequences of vertical acceleration were first observed in the early 1900s. In 1919, Head and Brown [1, 2] noticed a phenomenon known as “fainting in the air” caused by sustained airplane accelerations of 4.5 G’s or higher. Similar phenomena such as blackout and grayout were also observed around the same time. Over the coming decades, these effects became attributed to cessation of blood flow in the eyes and brain [3]. Since the technology did not yet exist to apply and then accurately measure accelerations large enough to cause dramatic injuries, early research on the response of humans to vertical accelerations focused on non-life-threatening acceleration levels. In the 1950s, research began to evolve that resulted in designation of a range of acceleration thresholds that could cause severe injury and death. Investigators began to understand that rapid vertical acceleration could cause, in addition to blackout and unconsciousness, fracture of the spinal cord, and brain contact with the skull. Stoll [4] determined that the severity of human response to vertical acceleration depends not only on maximum acceleration, but also the rate that acceleration is applied. Later, Eiband [5] published data showing the effects of acceleration on scales smaller than previously investigated. He also

Electronic supplementary material The online version of this article (doi:10.1007/s11340-013-9834-2) contains supplementary material, which is available to authorized users.

X. Zhao (✉) · G. Shultis · M. Sutton · X. Deng
Department of Mechanical Engineering, University of South
Carolina, Columbia, SC 29208, USA
e-mail: zhao29@email.sc.edu

R. Hurley · W. Fourney · U. Leiste
Department of Mechanical Engineering, University of Maryland,
College Park, MD 20742, USA



developed graphs illustrating the vertical acceleration tolerance thresholds of human beings. Gurdjian and co-workers [6–8] first proposed the “Wayne State University Cerebral Concussion Tolerance Curve (WSTC)”. Based on the curve, an important severity index was developed which is known as Head Injury Criterion (HIC). In 1969, Stech [9] proposed another injury criterion Dynamic Response Index (DRI). The DRI is a model that assesses the physical response of the human body to upward acceleration and is based on a differential equation describing the stiffness of the spinal cord. In the following decades, a variety of other head injury criteria had been proposed and investigated [10–13]. The Department of Defense (DoD) and U.S. Army have developed limiting thresholds for human vertical acceleration tolerance based on the WSTC and other research studies. The DOD has suggested limiting human acceleration to 25G for 100 ms [14]. The U.S. Army has suggested a limit of 23G for 25 ms [15], where G is the acceleration of gravity. The National Highway Traffic Safety Administration (NHTSA) specified the limit for HIC evaluated over a maximum time interval of 36 ms for the 50th percentile male. As of 2000 [16, 17], the NHTSA final rule adopted limits that reduce the maximum time for calculating the HIC from 36 ms (HIC_{36}) to 15 ms (HIC_{15}). The NHTSA final rule also revised the HIC limits for different sizes of dummies. The HIC value is calculated using Eq. (1).

$$HIC = \max \left\{ (t_2 - t_1) \left[\frac{1}{t_2 - t_1} \int_{t_1}^{t_2} a(t) dt \right]^{2.5} \right\} \quad (1)$$

where $a(t)$ is the acceleration (expressed in G), and $(t_2 - t_1)$ is the time interval (expressed in s). The HIC_{15} metric was used in these studies, consistent with the requirements of the National Highway Traffic Safety Administration (NHTSA). Details regarding the procedure used to compute HIC_{15} will be presented in Section 6.2.

Regarding the investigations on buried blast loading experiments, Nurick and Shave [18] experimentally studied the failure of thin edge clamped steel plates subjected to explosive loading by using a ballistic pendulum. The authors estimated the total impulse and analyzed the type of failure mode experienced by the clamped plate. Jacob et al. [19] reported a series of experimental results and numerical predictions for clamped mild steel quadrangular plate of different thickness and varying length-to-width ratios subjected to localized blast loads of varying size. They introduced a localized loading parameter to the dimensionless damage number to simplify the complexity of interaction between charge diameter and plate geometry and compared with the results in Ref. [20] with good success. Later, they [21] studied the effect of stand-off distance and charge mass on the response of fully clamped circular mild steel plates using blast tube and indicated that blast loading is

localized or uniformly distributed depending on the ratio of stand-off distance to diameter of plate. Fournay and his co-authors [22–24] performed a series of buried blast experiments to quantify the effect of parameters. In some cases, when the soil is saturated sand, there were explosive ‘bubble’ effects similar to those encountered in shallow water. Schleyer et al. [25] reported the response of the panel, which was based on a deep trough trapezoidal profile with welded angle connections at the top, bottom and free sides, loaded by the shocked pressure pulse representative of the positive phase of the air blast loading arising from a high-explosive charge. Lawrence [26] and Hargather [27] reported photographic studies on the mechanism of detonation in explosives and the scaling of blasts respectively. Tiwari et al. [28] measured the full-field transient plate deformation of a limited specified center area during blast loading by using 3D image correlation. In Snyman’s work [29], he showed the similarity of the imparted impulse of different shape of charges obtained by the horizontal motion of a pendulum. Fox et al. [30] performed computational investigations of rigid targets with various geometries to the detonation of shallow buried explosives and compared to experiments with good agreement. It is noted that these related experimental studies primarily focused on dynamic behavior of a single unprotected plate subjected to high rates of loading.

In this study, small scale model experiments employing both a passenger floorboard and external frame support with lower V-shaped hull were designed and manufactured via *input-based scaling of full sized components*. The effects of various hull modifications on measured vertical acceleration are presented. In addition, HIC_{15} values calculated from experimental results using Eq. (1) are employed to assess the merits of various mitigation strategies for protecting personnel.

Input Scaling of Experimental Structure Configuration

Recent studies have shown that the full specimen-explosive-structure scaling via dimensional analysis can be used to accurately predict the deformation response of appropriately scaled blast loading structures [31–36]. For blast loading studies, dimensional analysis [37–40] has shown that a scaling factor can be derived from the cube root of the ratio of the full size charge mass to the small scale charge mass.

Even when complete scaling of the structure is not feasible, small scale experiments are oftentimes performed using a smaller amount of explosive, and the results used to estimate the behavior of full-scale structures. In our studies, the investigators scaled the explosive weight (input scaling) and approximately scaled various structural elements using a 1/3 scaling law [31, 32] to be nominally consistent with large-scale structures. As shown in Eq. (2), the scaling factor $\beta =$

10.102 was used in our studies unless otherwise noted, so that detonation of 1.031 kg of Pentaerythritol Tetranitrate (PETN)

explosive for a full-scale vehicle corresponds to detonation of a 1 g PETN explosive in these experiments (see Eq. (2)).

$$\beta = \left(\frac{m_{full}^{expl}}{m_{small}^{expl}} \right)^{1/3} = \left\{ \begin{array}{l} \left(\frac{1031g}{1g} \right)^{1/3} \text{ --- Exps 1-17 in Part I} \\ \left(\frac{4536g}{4.4g} \right)^{1/3} \text{ --- Exps 18-26 in Part II} \end{array} \right\} = 10.102 \quad (2)$$

For partial scaling such as performed in these studies, Eq. (3a), (3b), (3c) and (3d) are approximate relationships between time, distance (e.g., depth of burial (DoB)), velocity and acceleration, respectively.

$$\frac{t_{full}}{t_{small}} \cong 10.102 \rightarrow t_{full} \cong 10.102 t_{small} \quad (3a)$$

$$\frac{DoB_{full}}{DoB_{small}} \cong 10.102 \rightarrow DoB_{full} \cong 10.102 DoB_{small} \quad (3b)$$

$$\frac{v(t)_{full}}{v(t)_{small}} \cong 1 \rightarrow \mathbf{v}(t)_{full} \cong \mathbf{v}(t)_{small} \quad (3c)$$

$$\frac{a(t)_{full}}{a(t)_{small}} \cong \frac{1}{10.102} \rightarrow a(t)_{full} \cong \frac{a(t)_{small}}{10.102} \quad (3d)$$

Thus, a 7.62 mm DoB of 1 g of PETN explosive in our small scale experiments would correspond approximately to 77 mm DoB of 1.031 kg of PETN explosive in full-sized structures. Details regarding the relationship between small-scale parameters and their full scale equivalents are shown in Table 1.

Experiments

Two independent sets of experiments were performed. The first set focused on the effects of hull type/shape on the mitigation of **floorboard motions and accelerations** in small scale model structures emulating reduced weight aluminum vehicles; the application of interest relates to the effect of floorboard motions during blast loading on passengers in contact with floorboards in nominally aluminum structures. In these studies, 3D digital

image correlation was used to measure floorboard motions, velocities and accelerations during blast loading.

A second set of experiments will be presented in Part II and focuses on **frame motions and accelerations** when steel frames and steel structures are employed with various frame connections and coatings for frame blast mitigation. In addition, direct comparison of measurements using 3D-DIC and accelerometers are reported in a companion article, Part II, which shows that the data obtained using 3D-DIC is as accurate as the data obtained using accelerometers. Furthermore, the 3D-DIC data was obtained successfully in all cases whereas the accelerometers failed in multiple blast loading experiments.

Measurement of Floorboard Deformations during Blast Loading Using Stereovision Digital Image Correlation

Figure 1 shows a schematic of the overall experimental configuration, including cameras, specimen-frame combination and sand blast facility. The setup consists of two matched Vision Research Phantom V12.1 high speed digital cameras. The cameras' optical arrangement used in the experiments has the following overall configuration;

- total pan angle between two optical axes $\approx 52^\circ$
- distance from the lens to the center of plate ≈ 1.2 m
- spacing of the calibration grid ≈ 12 mm
- lens focal length ≈ 50 mm; lens F stop number ≈ 8
- 8 bit image intensity quantization

Table 1 Relationship between small scale and full-scale parameter values for blast loading experiments

	Small size test	Full size test
DoB (depth of bury)	7.62 mm	77.0 mm
SoD (stand-off distance)	81.0 mm	817.88 mm
Vehicle length	406.4 mm	4105.45 mm
Vehicle width	355.6 mm	3592..27 mm

Scale factor is 10.102, representing scaling up to combat vehicle size

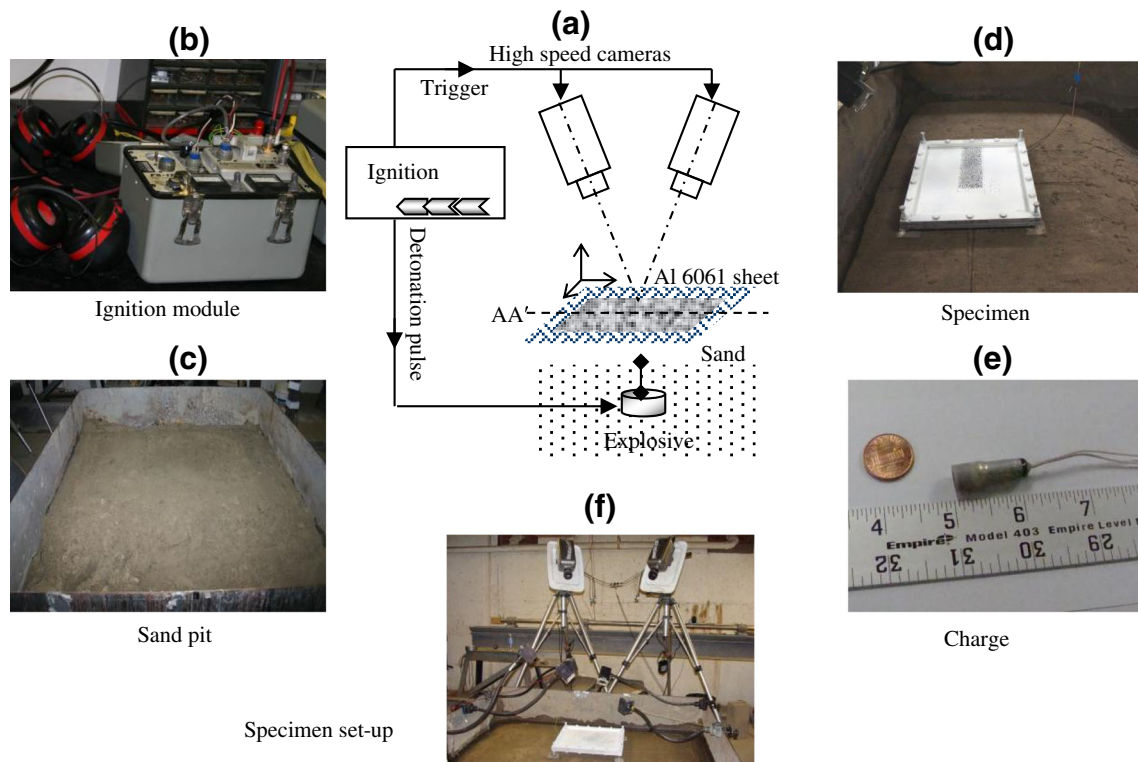


Fig. 1 Experimental set-up for buried blast loading experiments

- cross-camera synchronization within $\pm 1 \mu\text{s}$ using external TTL pulse
- lighting using multiple halogen lamps attached to concrete walls
- image sizes ranging from 48×256 pixels to 64×368 pixels
- inter-frame time ranging from $3.36 \mu\text{s}$ to $5.49 \mu\text{s}$

For the magnification of interest, a high contrast random speckle pattern is placed on the specimen center area that is undergoing maximum deformation and acceleration when exposed to central region detonation. The specimen was lightly coated with white enamel paint and then a sharpie marker was used to manually apply a dot pattern of the appropriate size and distribution on the specimen. Once the specimen is assembled to the frame fixture, threaded spacers are affixed at the four corners of the fixture. The height of the spacers is adjusted to meet the stand-off distance (SoD) to be used in the experiment. The assembled experimental configuration is temporarily placed on the sand surface and the outer edge of the frame carefully etched into the sand surface, with the center location identified using diagonal lines. The specimen is then removed and the explosive charge and detonator are assembled and carefully buried in the sand below the center location and at the appropriate depth of bury (DoB).

After the explosive is buried, the cameras are mounted on tripods and oriented to view the position where the specimen will be located. Calibration images of a grid located near the buried explosive are obtained. The calibration grid images are

used to verify that a convergent calibration analysis is obtained. After calibration has been confirmed, the cameras are covered with plastic protective enclosures to mitigate impact from sand or other debris expelled during blast loading. The plastic protective enclosure was fabricated using a high quality, flat transparent and thin ($< 1 \text{ mm}$) epoxy plate, with the front plate approximately orthogonal to the optical axis of the lens. In such cases, addition of the plate should not affect the calibration process and will have minimal effect on the measurements. Finally, the specimen is replaced above the buried charge and the SoD is again confirmed prior to initiating the blast loading. Once a final check is performed, the laboratory is evacuated and two simultaneous electric pulses are sent to the detonator to initiate the explosion and simultaneously trigger both cameras to record the event.

Floorboard Measurements in Aluminum Frame-Hull Structures

The aluminum alloy Al6061-T6 is used to manufacture the floorboards, frame and hulls for all experiments. Details for all experiments are given Tables 2 and 3. Figures 2 and 3 shows a top view (Fig. 2(a)), side view of specimen-frame structure without a hull (Fig. 2(b)) and several side views (Fig. 2(c~h)) of all the V-shaped hulls used in the first set of experiments listed in Table 2. The specimen and hulls are bolted onto an

Table 2 List of experiments with Aluminum frame measured by high-speed cameras

Exp. #	DoB (mm)	SoD to floorboard (mm)	Charge (grams)	Floorboard and Al6061 frame dimensions (mm)	Al6061 Floorboard thickness (mm)	Hull	Al6061 Hull thickness (inches)	Angle of hull (degrees)	Image size (pixels)	1/FPS* (μ s)	Detonator
1	7.62	81.0	1	355.6×406.4	0.51	No hull	None	None	256×64	4.34	RP80
2	25.4	81.0	1	355.6×406.4	0.51	No hull	None	None	384×56	4.80	RP80
3	25.4	81.0	1	355.6×406.4	0.51	Single hull	2.29	13/154/13	512×48	5.07	RP80
4	12.7	81.0	1	355.6×406.4	0.51	Single hull	2.29	13/154/13	512×48	5.07	RP80
5	7.62	81.0	1	355.6×406.4	0.51	Single hull	2.29	13/154/13	368×64	5.49	RP80
5R*	7.62	81.0	1	355.6×406.4	0.51	Single hull	2.29	13/154/13	368×64	5.49	RP80
6	7.62	81.0	1	355.6×406.4	0.51	Foam and single hull	2.29	13/154/13	512×48	5.07	RP80
7	7.62	81.0	1	355.6×406.4	0.51	Double hull	2.29	13/154/13	400×48	5.13	RP80
8	7.62	81.0	1	355.6×406.4	0.51	Cantilevered single hull	2.29	13/154/13	384×56	4.80	RP80
9	7.62	81.0	1	355.6×406.4	0.51	Cantilevered single corrugated hull	2.29	13/154/13 40/100/40	256×48	3.36	RP80
10	25.4	81.0	1	355.6×406.4	0.51	Corrugated hull	2.29	13/154/13 40/100/40	384×48	4.23	RP80
11	7.62	81.0	1	355.6×406.4	0.51	Corrugated hull	2.29	13/154/13 40/100/40	384×48	4.23	RP80
12	7.62	81.0	1	355.6×406.4	1.60	Corrugated hull	2.29	13/154/13 40/100/40	256×48	3.36	RP80
13	7.62	81.0	1	355.6×406.4	1.60	No hull	None	None	384×56	4.80	RP80
14	7.62	31.0	1	355.6×406.4	1.60	No hull	None	None	384×56	4.80	RP80
14R*	7.62	31.0	1	355.6×406.4	1.60	No hull	None	None	384×56	4.80	RP80
15	25.4	31.0	1	355.6×406.4	1.60	No hull	None	None	384×48	4.23	RP80

R* —Repeated experiment

1/FPS*—Since camera resolution is a function of frame rate, the frame rate used in each experiment was changed slightly for high-speed Phantom cameras to maintain approximately the same number of pixels/mm for the as-applied speckle pattern. Since these slight changes in frame rate give essentially the same pixels/mm for the speckle pattern, when using the same subset size this approach maintains similar 3D-DIC accuracy for all experiments

aluminum frame that consists of two geometrically identical parts; upper clamping member and lower frame. The lower rectangular frame has outer dimensions of 355.6 mm×406.4 mm×12.7 mm, and an inner cutout opening with dimensions 304.8 mm×355.6 mm. The rectangular shape for the lower frame and clamping member are constructed using pieces from a 25.4 mm×12.7 mm aluminum bar stock welded at the corners. Each half of the frame is machined with 18–9.525 mm diameter matching holes.

The specimen has a similar set of 18 holes and is bolted between the two frames using 9.525 mm diameter stainless steel bolts, lock washers and stainless steel nuts.

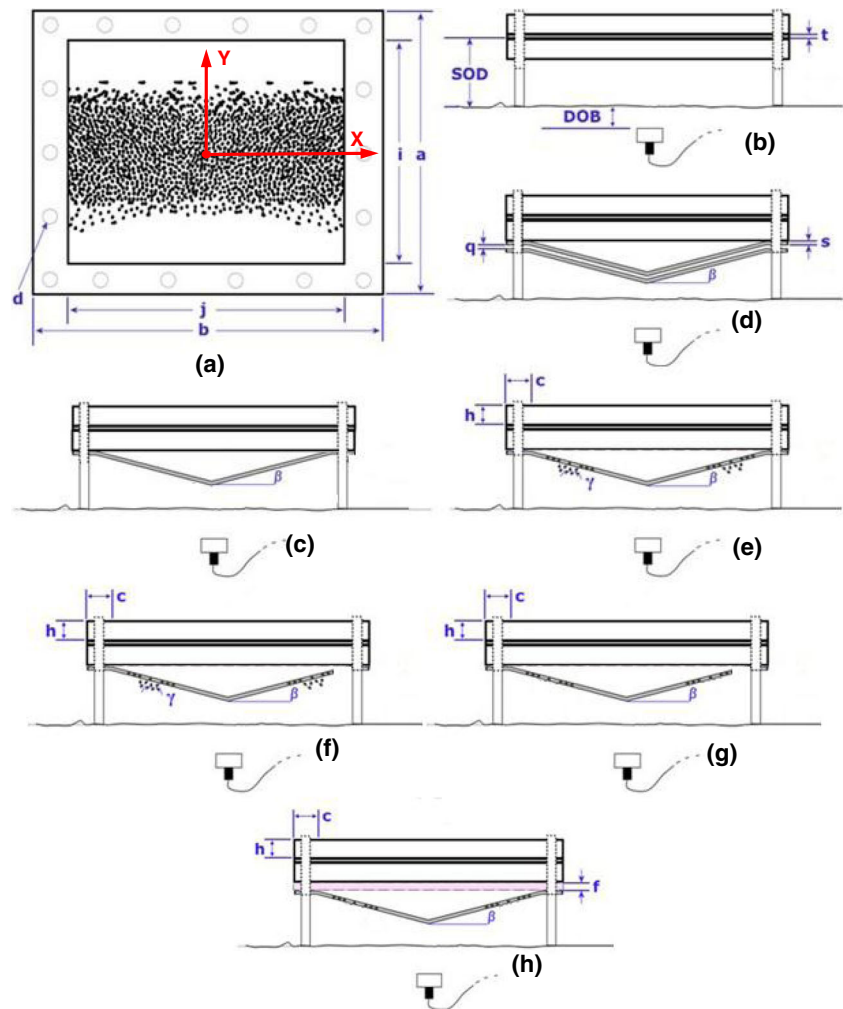
Velocity and Acceleration Determination of Floorboard

For all standard hulls with frames and floorboards (see Table 2), the out-of-plane displacement, U_z which is in the Z direction, of

Table 3 List of experiments with steel frame measure by high-speed cameras

Exp. #	DoB (mm)	SoD to floorboard (mm)	Charge (grams)	Floorboard and steel frame dimensions (mm)	Al6061 Floorboard thickness (mm)	Hull	Al6061 Hull thickness (inches)	Angle of hull (degrees)	Image size (pixels)	1/FPS (μ s)	Detonator
16	7.62	31.0	1	355.6×406.4	1.60	No hull	None	None	128×128	5.07	RP80
17	25.4	31.0	1	355.6×406.4	1.60	No hull	None	None	128×128	5.07	RP80

Fig. 2 Specimen and frame configurations with and without hulls: **a** floorboard alone; **b** no hull; **c** single hull; **d** double hull; **e** corrugated hull; **f** cantilevered single corrugated hull; **g** cantilevered single hull; **h** frame foam padding with single hull. In figure: $d=9.53$, $b=406.4$, $j=355.6$, $i=304.8$, $a=355.6$, $t=0.51$, $h=12.7$, $c=25.4$, $q=4.57$, $f=8.89$, $s=2.29$, $\gamma=100^\circ$ (including angle of corrugation), $\beta=13^\circ$. (unit: mm)



the center-point location (0,0,0) in each floorboard is measured using 3D digital image correlation; all three displacement components are measured, but only U_z is used in this study¹. Out-of-plane velocity and acceleration results at the center-point are obtained by differentiating the out-of-plane displacement U_z time history in the following way. First, a time series of data for $U_z(x,y,t)$ is obtained at every time interval; the component U_z will be used in the following discussion. Second, using this time sequence for U_z , a “moving window least squares quadratic fit” is performed in time to seven consecutive data points, beginning with the data at time t_0 . Third, the quadratic fit is differentiated (a) once to obtain the velocity at the midpoint of the time span and (b) twice to obtain the acceleration at the midpoint of the time span. This process is repeated by moving forward in time Δt and selecting seven consecutive points starting at time $t_0 + \Delta t$, continuing until the entire velocity and acceleration

history is obtained for a point of the plate. Then, velocity $\partial U_z / \partial t(t)$ and acceleration $\partial^2 U_z / \partial t^2(t)$ time histories, are filtered using an FFT with a Butterworth low pass filter having a 10 kHz cutoff frequency to remove high frequency, low amplitude oscillations that occur later in the time period. A typical filtered experimental data is shown in Fig. 4. Direct comparison of filtered data and unfiltered data for both velocity and acceleration data confirm that the filtering process does not have an appreciable effect on the velocity and acceleration results.

Hull Systems

The weight of Army Ground Combat Vehicle keeps growing due to increased threats to passengers from blast events and more lethal weapon systems. The current total weight of ground vehicles can exceed 70 t contributed by armor protection employed to mitigate blast effects, at the cost of reduced mobility and speed, increased fuel consumption and decreased transportability. Concern regarding these issues has resulted in DoD mandates to give serious consideration of

¹ Review of video data indicates that each plate-frame structure moves upward rigidly, with minimal rotation, during the first 36 ms after initial detonation. This was true for all experiments performed in this study.

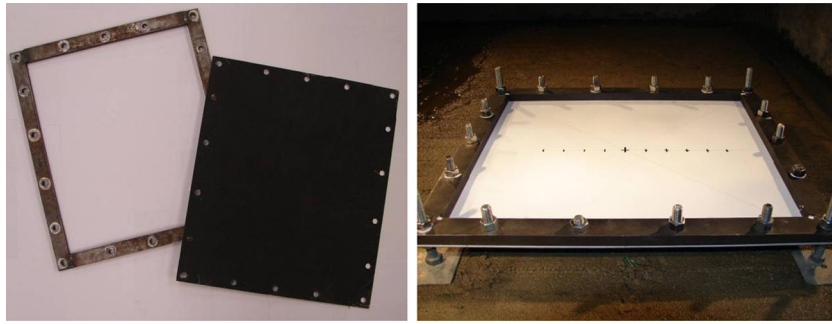


Fig. 3 Floorboard and steel frame specimen for experiments 16 and 17 with no hull. The steel frame was constructed by welding 12.7 mm by 25.4 mm steel stock into a rectangle and drilling the 18 holes with 9.525 mm diameter for holding the plate. The dimensions of frame are 12.7 mm thickness, 25.4 mm width, 355.6×406.4 mm external dimension, which are same as aluminum frame used in Experiments 1-15

ways to decrease weight while maintaining reasonable levels of protection and cost. Thus, protective hulls remain an important contributor to overall vehicle safety while adding a minimum of weight to the structure. As shown in Fig. 2 and Table 2, four types of small scale hull designs are evaluated experimentally. In one experiment, rigid foam was also employed. Details for each design are provided in the following sections.

Single Hull

The standard single hull is shown in Fig. 2(c). The optimum bending angle (measured along an axis parallel to the floorboard and along the long side of the frame) for each side of the hull is between 13° and 20° [41–43]. Though delivering similar amounts of transmitted impulse, a 13° angle is preferred to maximize distance between the floorboard and the ground.

In these studies, each hull is shaped with a 13° bend on each side, culminating in a total angle of 26° and a 154° V

shape, returning symmetrically back to the original height for the opposing 13° bend. For the standard case hull, the original sheet is cut to dimensions of 368.3 mm×406.4 mm. The width reduces to 355.6 mm after introducing the hull bends.

Double Hull

The double hull is shown in Fig. 2(d). The double hull is constructed from two standard single hulls combined in one experiment. The process for creating them is exactly the same. However, the double hull specimens are mounted differently on the specimen. Larger bolts are required to pass through the extra material. The larger bolts and the extra hull increased the overall weight of the structure. Furthermore, a 4.57 mm spacer is placed between each hull on both sides of the specimen to ensure the floorboard and lower hull do not interfere during the early stages of the blast. Interference between the two hulls will transfer load across the contact region, altering the behavior of the double hull system.

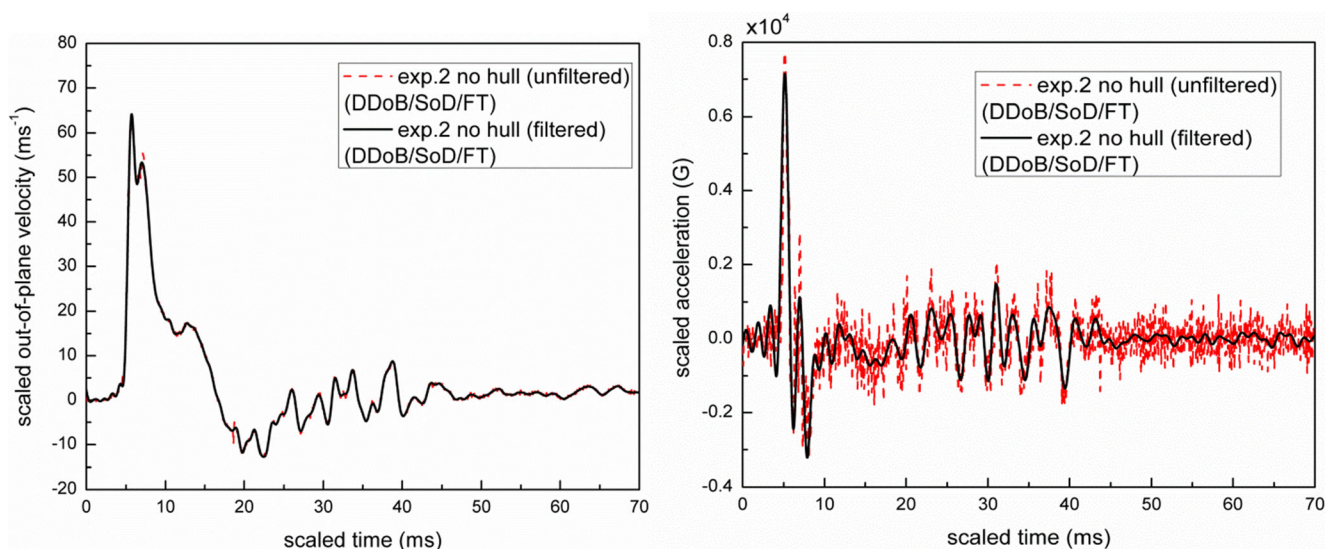


Fig. 4 Filtered out-of-plane velocity and acceleration data of floorboard center. (DDoB-25.4 mm, SoD-81 mm, FT-0.51 mm floorboard)

Corrugated Hull

The corrugated single hull design is shown schematically in Fig. 2(e). The corrugated hull is considered as a simple approach for increasing flexibility and energy absorption, reducing transmission of energy into the frame and floorboard. The corrugated hull has the same dimensions as the standard single hull, with the exception of the introduction of the corrugation at a distance 87.12 mm (3.43 in. from the center of the hull). The initial flat plate has a size of 393.7 mm × 406.4 mm. An additional 38.1 mm is needed due to the shaping of the hull, with 25.4 mm specifically for corrugation.

Cantilever Hulls

Figure 2(f) and (g) show the geometry of the cantilevered single and single corrugated hulls, respectively. In each case, the hull is attached along one side, unrestrained on the other side, and has an initial clearance of 12.7 mm on the unrestrained side.

Rigid Foam and Single Hull

A specific experiment focused on the effect of rigid foam padding between the frame and a single V-shaped hull is performed. In these studies, a foam thickness of 8.89 mm is used. The foam padding and single hull, shown in Fig. 2(h), has a bolted connection through the hull, frame and floorboard. The foam padding and frame widths are the same.

Experimental Results

Unless otherwise noted, the measured time, displacement, velocity and acceleration measurements were “input-scaled” according to Eq. (2a-2d) so that the presentation will correspond approximately to the expected full-scale results for similar structures with 1.031 kg of PETN explosive.

To demonstrate the consistency of the blast loading methodology with 3D digital image correlation measurements, experiment 5 in Table 2 was repeated using the same DoB, SoD, charge mass, aluminum frame, hull and floorboard dimensions and image resolution. The measured center point displacement data on the floorboard for both experiments are compared in Fig. 5. As shown in Fig. 5, the peak in displacement occurred ≈ 2 ms after detonation in both cases while a minimum in displacement occurred ≈ 3.5 ms after detonation in both cases. Figure 6 compares the residual deformation of the floorboard along the plate center line at $y=0$ for both specimens measured by 3D digital image correlation. As shown in Fig. 6, the measurements have maximum and minimum values at nearly the same time and show nearly identical trends for all other points. Taken together, the data shown in Figs. 5 and 6 appears sufficiently similar in a dynamic and difficult-to-control

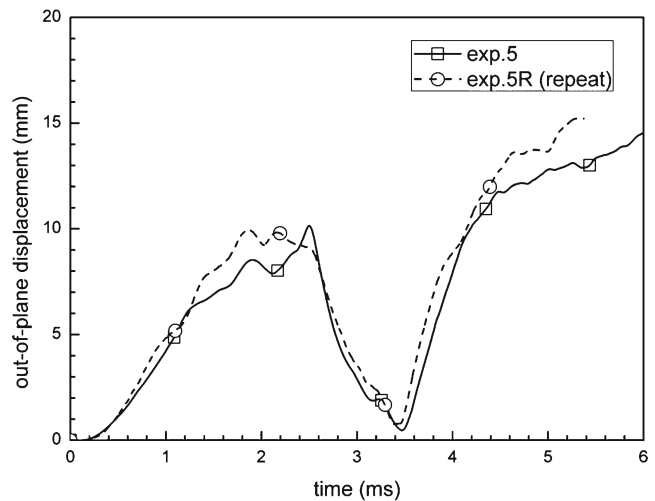


Fig. 5 Un-scaled out-of-plane displacement at approximate floorboard center location

environment to demonstrate repeatability of the experiments and consistency in the stereovision measurements.

Out-of-plane Motions of Floorboard Center

Input-scaled displacement histories for typical floorboard center-point out-of-plane displacements in Experiments 1, 2, 3, 5, 8, 10 and 13 are shown in Fig. 7. Results for the remaining experiments are given in Appendix A-1.

The procedure described in Section 5.1 is used to determine the input-scaled acceleration histories for the floorboard center location, with and without various protective hulls. Maximum input-scaled vertical acceleration results during the first 15 ms are presented in Fig. 8. The complete input-scaled acceleration histories of the floorboard center location are given in Appendix A-2. The input-scaled peak values for the out-of-plane displacement, acceleration and HIC_{15} at the floorboard center showed in Figs. 7, 8, and 9 and summarized in Table 4.

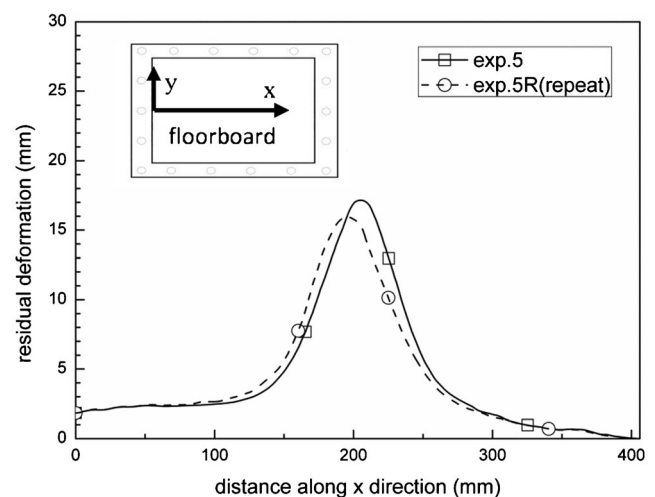
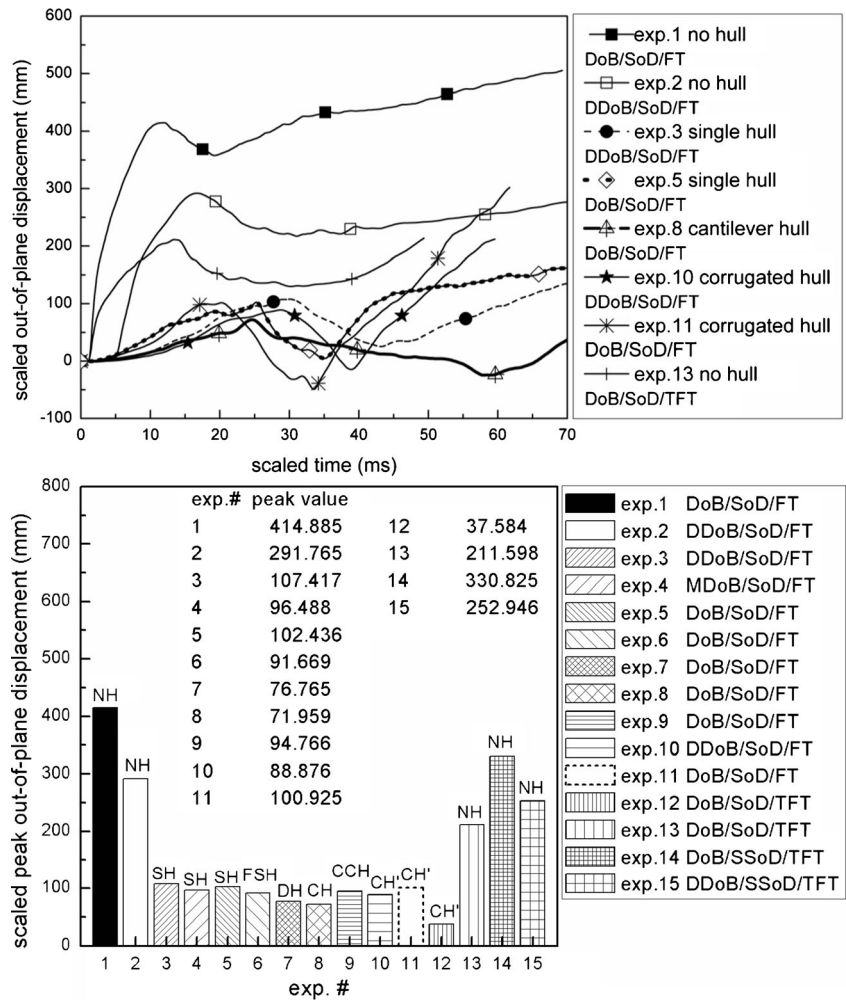


Fig. 6 Un-scaled residual shape along x direction

Fig. 7 Input-scaled out-of-plane displacement histories of experiments 1, 2, 3, 5, 8, 10, 11 and 13 (top), and peak value of out-of-plane displacements of all experiments at floorboard center location (bottom). (NH-no hull, SH-single hull, FSH-foam & single hull, DH-double hull, CH-cantilever hull, CCH-cantilever single corrugated hull, CH'-corrugated hull, DoB-7.62 mm, MDoB-12.7 mm, DDoB-25.4 mm, SoD-81 mm, SSoD-31 mm, FT-0.51 mm floorboard, TFT-1.60 mm floorboard)



HIC₁₅ Measurements

The procedure to obtain HIC₁₅ values using Eq. (1) is given in Appendix A-3. Figure 9 shows the input-scaled maximum

HIC₁₅ values. In addition, Appendix A-3 presents the complete time history of input-scaled HIC₁₅, providing information regarding the time frame where the maximum HIC₁₅ occurs.

Fig. 8 Input-scaled peak out-of-plane acceleration prior to peak negative acceleration of experiments 1 to 15 at approximate floorboard center location. (NH-no hull, SH-single hull, FSH-foam & single hull, DH-double hull, CH-cantilever hull, CCH-cantilever single corrugated hull, CH'-corrugated hull, DoB-7.62 mm, MDoB-12.7 mm, DDoB-25.4 mm, SoD-81 mm, SSoD-31 mm, FT-0.51 mm floorboard, TFT-1.60 mm floorboard)

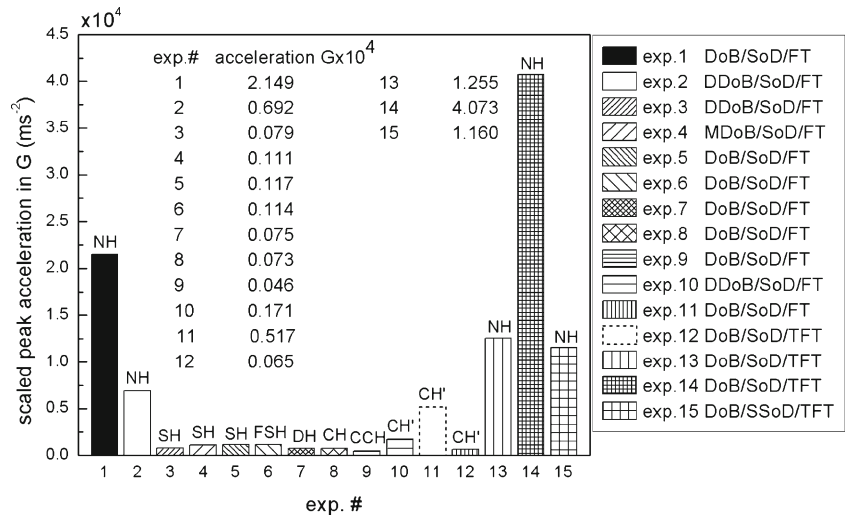
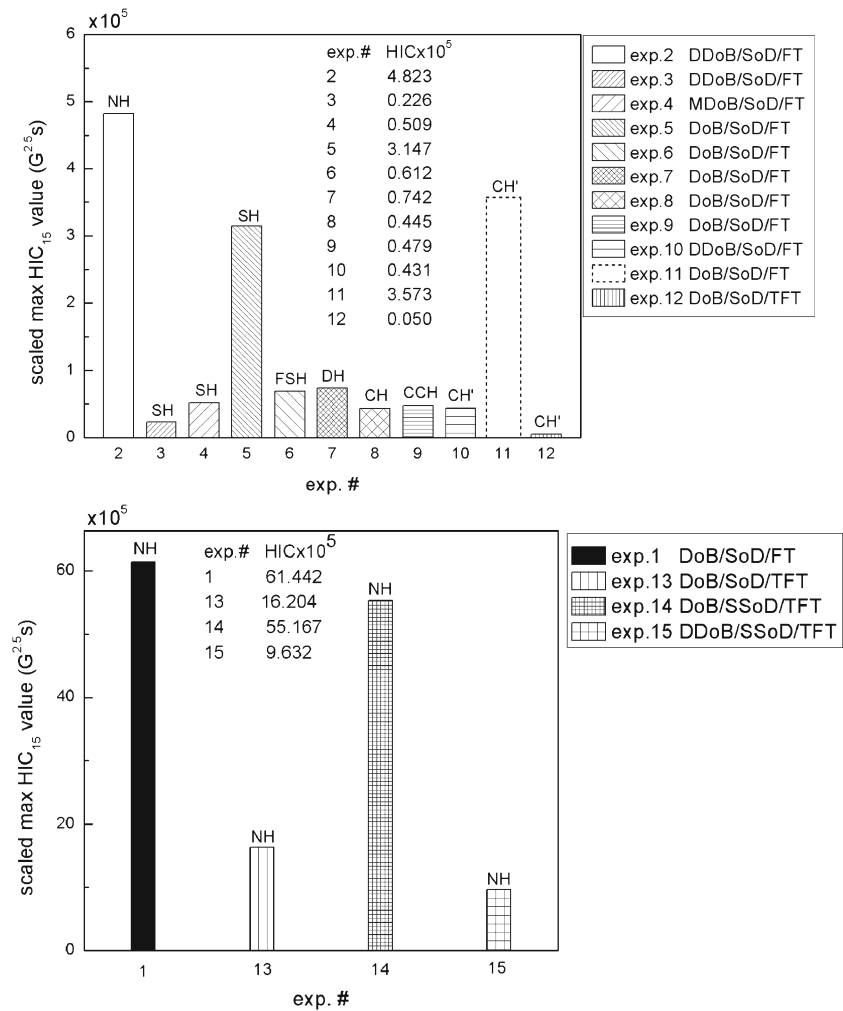


Fig. 9 Input-scaled maximum HIC_{15} value of experiments 1–15. (NH-no hull, SH-single hull, FSH-foam & single hull, DH-double hull, CH-cantilever hull, CCH-cantilever single corrugated hull, CH'-corrugated hull, DoB-7.62 mm, MDoB-12.7 mm, DDoB-25.4 mm, SoD-81 mm, SSoD-31 mm, FT-0.51 mm floorboard, TFT-1.60 mm floorboard)



Characteristics of a Buried Sand Blast Event

Figure 10 shows the evolution of failure in an unprotected floorboard after detonation of a 5 g buried explosive. Figure 11 show the back side of (a) a single V-shaped hull and (b) an unprotected floorboard after being subjected to a smaller blast event due to detonation of 1 g of explosive. Figure 12 shows a side-view of the ejected sand as it interact with a single V-shaped hull, with the separation and channeling effect of the hull clearly evident. The displacement and acceleration histories of the floorboard at locations ($X=0$, $Y=0$), ($X=513.2$ mm, $Y=0$) and ($X=769.8$ mm, $Y=0$) are shown (a) in Fig. 13 for an unprotected floorboard, (b) in Fig. 14 when using a standard V-shaped hull and (c) in Fig. 15 when using a cantilevered corrugated V-shaped hull.

Discussion

When employing various types of protective hulls, Fig. 7 and Table 4 show that the deflection of the floorboard center-point

is reduced by 6X relative to the no hull case for the same thickness of floorboard.

With regard to the results shown in Fig. 5, there are several points to be discussed. First, the blast loading process involves the entire hull-frame-floorboard structure, with different time scales relevant to the measured floorboard response. The actual blast loading process occurs on the time scale of microseconds, and the early time scale response of the floorboard is indicative of the localized response due to the blast process. Second, the longer time response which occurs on the scale of a few milliseconds is consistent with the complexity that arises when overall structural response ensues. Uploaded [video](#) evidence from side and top cameras shows the following: (a) Downward bending of the short side of the frame and upward bending of the long side of the frame occurs during first 2.2 milliseconds as the central region of the plate reaches a maximum upward out-of-plane displacement and the entire structure begins to lift off from the sand; (b) the structure deformations change to upward bending of the short side and downward bending of the long side from 2.2 ms to 3.4 ms, resulting in large downward motion of the attached

Table 4 Input-scaled peak values of out-of-plane displacement, acceleration and HIC_{15} at floorboard center

Exp. #	1	2	3	4	5	6	7	8	9	10	11	12	13	14	15
Out-of-plane displacement (mm)	414.885	291.765	107.417	96.488	102.436	91.669	76.765	71.959	94.766	88.876	100.925	37.584	210.598	330.825	252.946
Acceleration ($G \times 10^4$)	2.149	0.692	0.079	0.111	0.117	0.114	0.075	0.073	0.046	0.171	0.517	0.065	1.255	4.073	1.160
HIC_{15} ($G^{2.5} s \times 10^5$)	61.442	4.823	0.226	0.509	3.147	0.612	0.742	0.445	0.479	0.431	3.573	0.050	16.204	55.167	9.632

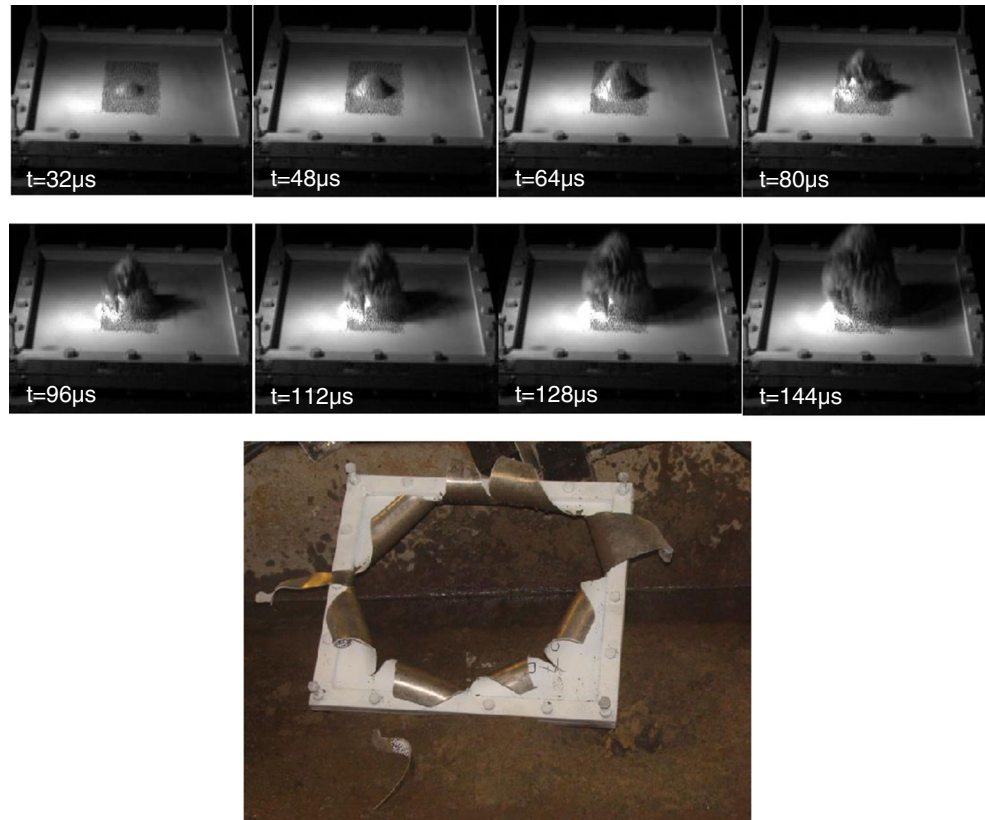
floorboard even as the entire structure moves upwards; it is believed that the sudden change in structural deformation is due in part to collapse of an air bubble generated during the buried blast loading process, resulting in very low pressure conditions below the hull; (c) Reverse elastic bending again occurs in the frame members, though with reduced amplitude, with the floorboard center moving upwards. During this time, a variety of small waves are clearly visible on the floorboard surface as oscillations and free vibrations continue.

It is noted that some displacement results shown in Fig. 7 have similar trends to those shown in Fig. 5. In addition, as shown in Fig. 7, the hull extends the period of time before the maximum in deflection occurs. This results in lower amplitudes for the floorboard acceleration and also delays the time for the peak value of acceleration. As shown in (a) Fig. 8 and (b) results for experiments 1–11 in Appendix A-3, hulls significantly reduce the measured center-point floorboard acceleration; the maximum acceleration is reduced by up to 47X. For a 0.51 mm thick aluminum floorboard, the magnitude of maximum floorboard acceleration range from 21490G (exp. 1 no hull) to 460G (exp. 9 cantilevered single corrugated hull). Though the relatively high acceleration magnitudes are well above the DoD limiting value (25G), they occur over a time period that is much less than the duration assumed to be necessary for biological damage (15 ms).

When simply using thicker floorboards without protective hulls, acceleration results in Fig. 8 show that increasing floor thickness does reduce accelerations but is not as effectively as V-shaped hulls. Specifically, a thickness increase of 312.5 % resulted in (a) a 1.7X reduction in acceleration when comparing experiment 13 to experiment 1 and (b) a 7.9X reduction in acceleration when comparing experiment 12 to experiment 11. However, as shown in Fig. 8, for experiment 12, the use of a corrugated hull with a thick floorboard results in a 20X reduction in acceleration relative to experiment 13, confirming that hull protection is a much more effective mitigator for a range of floorboard thicknesses.

In addition to the use of acceleration to assess blast severity, the Head Injury Criterion was calculated for different hull & floorboard or frame combinations using Eq. (1) and the procedure given in Appendix A-3. Though HIC_{15} does not specifically determine when a head injury would or would not have occurred in a victim, the metric does act as a guide to determine when head injury is most likely to have happened. By using consistent test and calculation methods, HIC_{15} values across multiple experiments can be compared to determine which conditions would be less likely to result in injuries. As shown in Fig. 9, for no-hull cases with floorboard thickness of 0.51 mm, the HIC_{15} values for the floorboard center-point range from 0.5 to $6 \times 10^6 G^{2.5} s$. These measured values are orders of magnitude larger than any current standard for minimizing head injury likelihood (e.g. DoD limit is $250 G^{2.5} s$, NHTSA limit is $700 G^{2.5} s$), suggesting that

Fig. 10 Evolution of floorboard rupture with no hull (Depth of bury-7.62 mm, Stand-off distance-31 mm, Explosive 5 g)



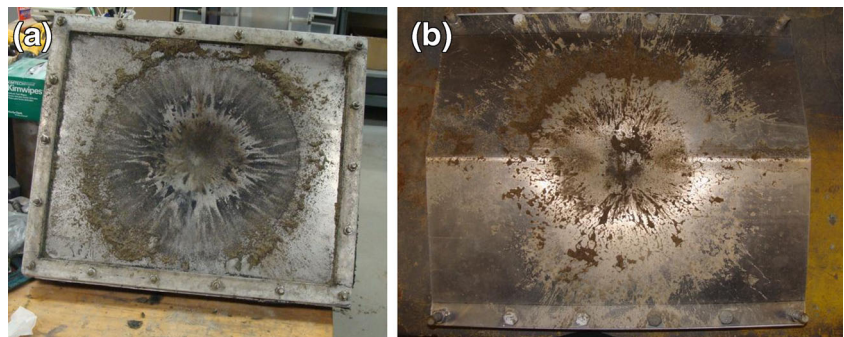
floorboard protection without hulls is insufficient to minimize passenger injury.

Regarding Head Injury Criterion, the time period (t_2-t_1) when acceleration occurs is considered in the HIC equation. The HIC value is used to estimate the maximum for the integrated or “average quantity” that humans can tolerate, although peak values exceed this “average” value. Conceptually, the HIC implies that even large accelerations may be “safe” as long as it occurs for a very short time. Conversely, even if the peak acceleration is not very large, it may be considered hazardous to health if it lasts for a longer time. Therefore, although the peak acceleration for experiment 9 is less than that measured for experiment 8, the time period of

peak acceleration in experiment 9 extends for a longer time than that in experiment 8, resulting in a slightly larger HIC value. The difference is due to corrugation on the hull which increases the time over which the blast loading effects are transferred to the structure and the floorboard

Since an important input variable for transmission of impulse to the hull-frame-floorboard structure is DoB, a direct comparison of the results for (a) experiments 5–9 with a constant DoB=7.62 mm and floorboard thickness $t=0.51$ mm and (b) experiments 12–14 with a constant DoB=7.62 mm and different floorboard thickness $t=1.6$ mm, are relevant. By comparing results from experiments 6–9 to results from experiment 5, the data indicates that additional

Fig. 11 Photographs of (a) back side of floorboard without protective hull after sand blast event and (b) bottom of V-shaped protective hull after sand blast event. (Depth of bury-7.62 mm, Stand-off distance-81 mm, Explosive 1 g)



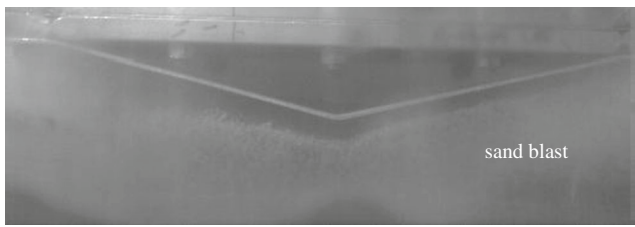


Fig. 12 Side view of ejected sand interacting with V-shaped hull during blast event

flexibility in the hull-frame connection via use of (a) foam or a spacer between the two single hulls or (b) removal of connections along one side reduces HIC by 4-7X. For experiments 12–14, results show that increasing floorboard thickness does decrease HIC, especially when combined with increased flexibility in the protective hull via corrugation of the hull.

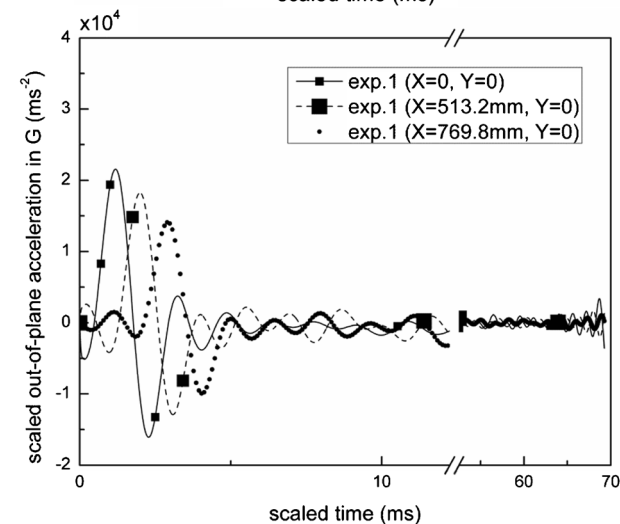
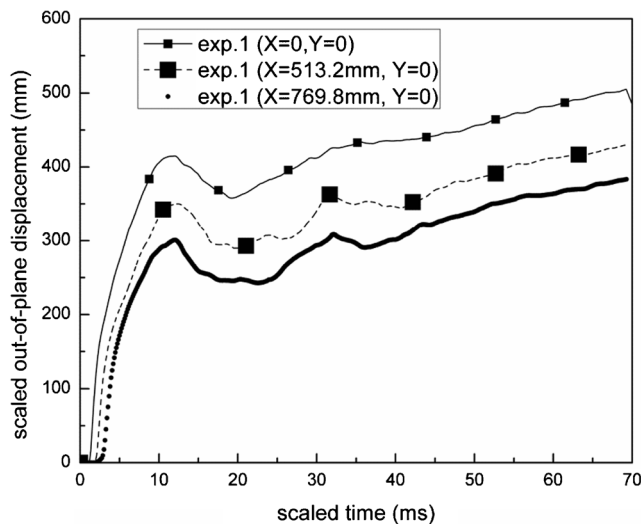


Fig. 13 Input-scaled out-of-plane displacements and accelerations at three different locations on unprotected floorboard identified in experiment 1

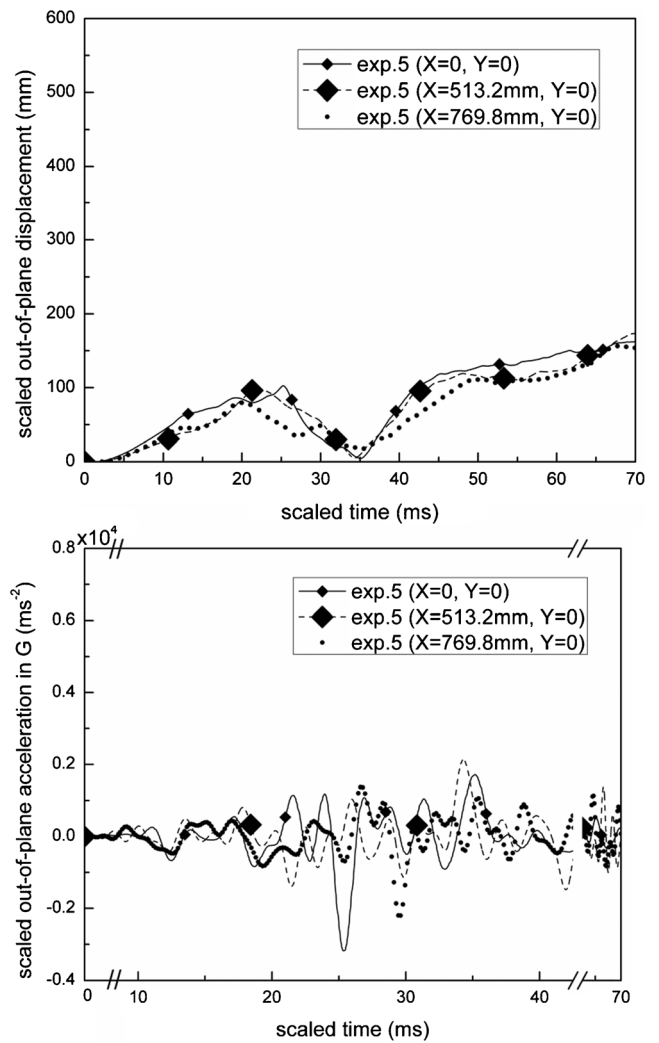


Fig. 14 Input-scaled out-of-plane displacements and accelerations at three different locations on floorboard protected by standard V-shaped hull identified in experiment 5

However, in practice this solution is unlikely to be viable due to the increased weight of the vehicle when using thicker floorboard structures.

For the same structure, the effects of DoB or SoD on HIC value are investigated by comparison of (a) experiments 3, 4 and 5 which have different DoB for the same SoD=81 mm and the same floorboard thickness $t=0.51$ mm, (b) experiments 14 and 15 which have different DoB for the same SoD=31 mm and floorboard thickness $t=1.6$ mm and (c) experiments 13 and 14 which have different SoD for the same DoB=7.62 mm and floorboard thickness $t=1.6$ mm. For the effect of DoB, experiments 3–5 and experiments 14–15 show that HIC₁₅ is reduced by 14X and 6X, respectively, from shallow buried explosives (DoB=7.62 mm) to deep buried explosives (DoB=25.4 mm). For the SoD effect, experiments 13–14 indicate that the maximum HIC₁₅ value increases a little more than 3X from high stand-off distance (SoD=

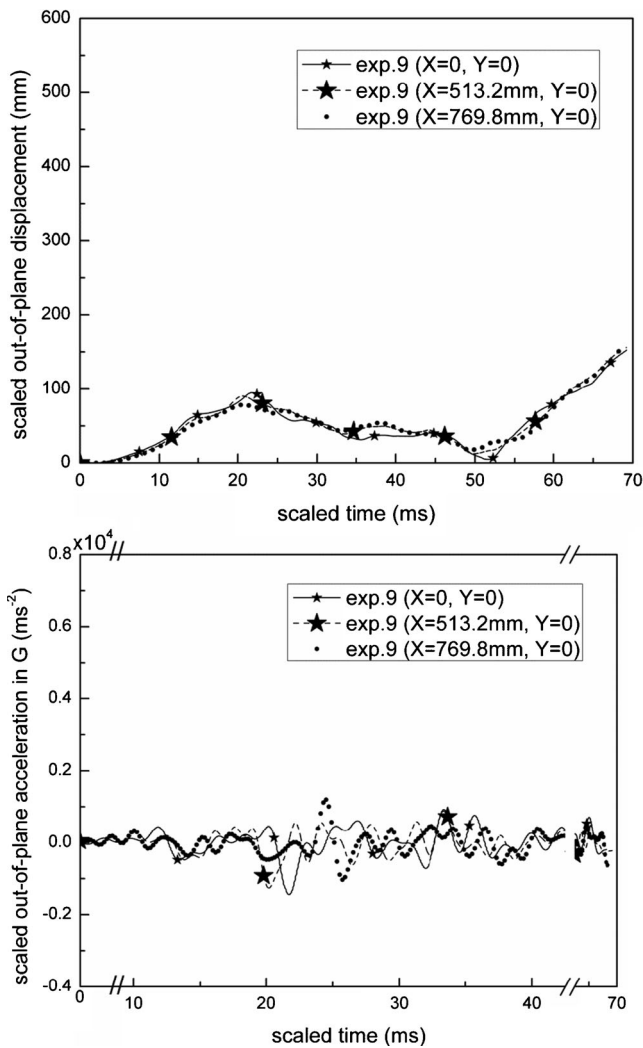


Fig. 15 Input-scaled out-of-plane displacements and accelerations at three different locations on floorboard protected by cantilevered corrugated hull identified in experiment 9

81 mm) to low stand-off distance (SoD=31 mm). Though it is conceptually feasible to increase the SoD to increase passenger safety, there are practical limits for SoD in real vehicles due to clearance requirements in the field.

As shown in Figs. 10 and 11, detonation of a lightly buried explosive result in contained damage on both unprotected floorboard and also a protective hull. The contained area of impact on the floorboard is also evident in the data shown in Fig. 13. Here, the amplitude of out-of-plane displacement and acceleration are reduced at locations which are further away from the floorboard center.

However, when a protective hull is employed, as shown in Fig. 12, the sand blast loading impacts the hull with load transfer distributed more broadly to the upper structure and the floorboard. The mitigating effect of hull is shown clearly in Figs. 14 and 15 where the amplitude of displacement and acceleration at different locations are relatively close to each other. Taken

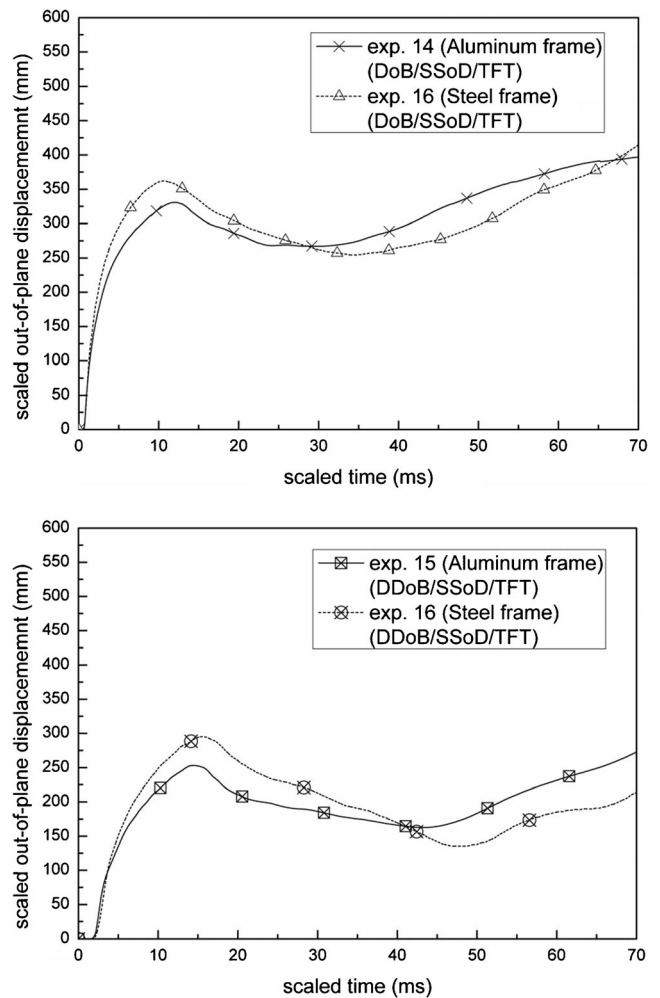


Fig. 16 Comparison of input-scaled out-of-plane displacement for center-point of floorboard using an aluminum and steel frame with DoB=7.62 mm (top) and input-scaled out-of-plane displacement for center-point of floorboard using an aluminum and steel frame with DDoB=25.4 mm (bottom). Aluminum floorboard thickness is TFT=1.60 mm in all cases and data scaled to full-size structure response. (SSoD=31 mm)

together, these results confirm that protective hulls distribute loading more broadly to the structure and the floorboard, thereby minimizing localization of damage to the floorboard. However, no matter whether there is a hull or not hull, the central region in floorboard remains the most affected, experiencing peaks in acceleration before rebound of floorboard that are quite high and sufficiently large so that serious or fatal injury may occur if occupants stand or walk within this area.

An overall review of the effect of hull effectiveness indicates that various protective mechanisms will reduce HIC_{15} measured on the floorboard by up to 128X. Even so, the minimum $HIC_{15}^{max} \approx 20 \times 10^3 G^{2.5} s$ (DoB=25.4 mm), which is nearly 2 orders of magnitude larger than the DoD limit. Based on this data, it is clear that efforts to mitigate standard floorboard accelerations to acceptable levels for human occupants will be difficult. A more appropriate design scenario

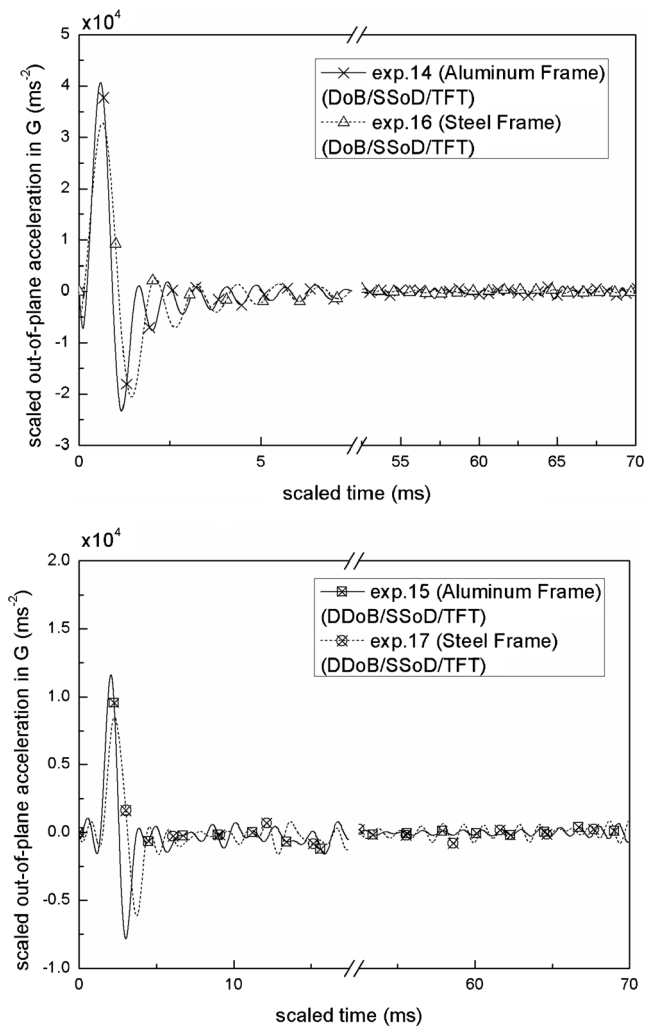


Fig. 17 Comparison of input-scaled out-of-plane accelerations (in G's) for center-point of floorboard using an aluminum and steel frame with DoB=7.62 mm (top) and input-scaled out-of-plane accelerations (in G's) for center-point of floorboard using an aluminum and steel frame with DDoB=25.4 mm (bottom). Aluminum floorboard thickness is TFT=1.60 mm in all cases and data scaled to full-size structure response. (SSoD=31 mm)

would be to consider situations where the occupant is attached to the external frame and to determine whether such situations may provide a more survivable situation.

An Alternative Structure to Increase Survivability of Passenger

With regard to the use of frame-mounted passenger seating to reduce the potential for injury, it is noted that most vehicles use steel structural frames. To obtain preliminary data and assess the effect of changing to a steel frame, the authors performed two buried explosive loading experiments (SoD=31 mm, DoB=7.62 mm and DoB=25.4 mm, 1 g PETN explosive) when using a steel frame. The steel frame and

floorboard dimensions used in the experiments are given in Table 3 and shown in Fig. 3. Designated experiments 16 and 17, the authors employed the same aluminum floorboard without benefit of a protective hull so that the results could be compared directly to data obtained in experiments 14 and 15 respectively, where an aluminum frame is used.

Figures 16 and 17 present direct comparisons of the measured out-of-plane displacement and acceleration at the plate center-point for (a) Exp 14 (aluminum frame) and Exp 16 (steel frame) with DoB =7.62 mm and (b) Exp 15 (aluminum frame) and Exp 17 (steel frame) with DoB=25.4 mm. Figure 18 present direct comparisons of the measured HIC₁₅ values at the plate center-point for Exp 14 and Exp 16 and Exp 15 and Exp 17, respectively.

Direct comparison of the results in Figs. 16, 17, and 18 clearly show that the change from an aluminum frame to a

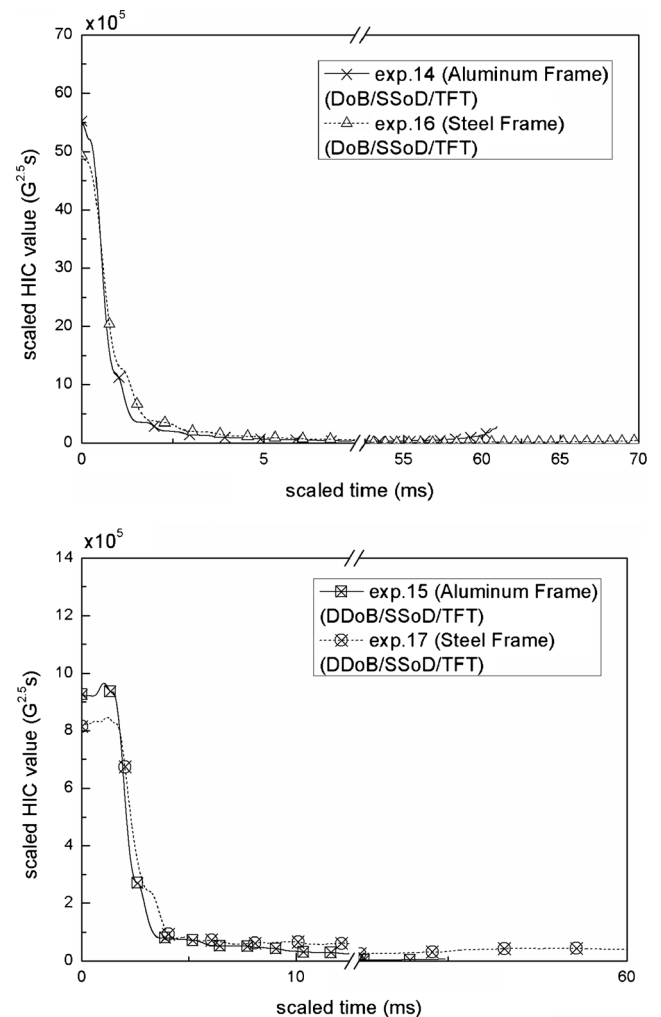


Fig. 18 Comparison of input-scaled HIC₁₅ values for center-point of floorboard using an aluminum and steel frame with DOB=7.62 mm (top) and input-scaled HIC₁₅ values for center-point of floorboard using an aluminum and steel frame with DOB=25.4 mm (bottom). Aluminum floorboard thickness is 1.60 mm in all cases and data scaled to full-size structure response. (SSoD=31 mm)

steel frame with somewhat different attachment procedure has minimal effect on the measured center-point acceleration and HIC_{15} values. Based on these results, as well as a general observation regarding the more common use of steel in frame structures, in Part II of our studies, the investigators will use the steel frame for all experiments.

Finally, as reported in detail in Part II of this work, to demonstrate that the 3D-DIC data is consistent with independent measurements, the authors attached accelerometers to the frame of several structures used in our experiments. Comparison of accelerometer and 3D-DIC measurements for the same region on the various frame structures demonstrated that the 3D-DIC data were in excellent agreement with accelerometer values in all cases where the accelerometer continued to function during the blast event.

Concluding Remarks

Single standard hulls use an optimized included angle of 154° in order to minimize the transmission of energy to the structure. The single corrugated hull employs similar geometry with corrugation to decrease stiffness and further reduce transmission. Unfortunately, under the same blast loading conditions as the single hull, the increased deformation of a single corrugated hull resulted in contact with the floorboard and increased energy transfer. Specifically, the results show that the corrugated hull does not decrease the measured floorboard acceleration.

Interestingly, by adding an additional degree of freedom through cantilevering of the corrugated and standard V-shaped hulls, data shows that this geometry change results in reductions in floorboard acceleration for both hulls. The cantilevered single corrugated hull performs somewhat better than a cantilever single hull in acceleration reduction because of the corrugation.

Finally, it is noted that increasing floorboard thickness is much less effective than using protective hulls for acceleration reduction. Moreover, thicker floorboards will result in increased total vehicle weight, which is unacceptable in practice.

In conclusion, results from our experiments clearly show that V-shaped hull structures with an optimized included angle of 154° are effective in reducing structure acceleration and associated human injury metrics, especially the cantilevered single corrugated hull. For the same DoB, use of a cantilevered single corrugated hull (experiment 9) reduces the peak value of deflection by 4X, acceleration by 47X and HIC_{15} by 128X when compared to the case with no hull (experiment 1). However, even though the V-shaped hull with the optimum bend angle does significantly reduce accelerations relative to the no-hull configuration, the resulting floorboard accelerations are still be too large to prevent serious injury. Thus, the safety of passengers in a vehicle subjected to the effects of an IED

explosive blast also relies heavily on internal human seat positioning and attachment. As a result, the focus of the research in Part II is to quantify the accelerations of a frame structure and ascertain the effectiveness of frame-mounted passenger seating in reducing passenger injury metrics.

Acknowledgments The technical support of Dr. Bruce Lamattina and the financial assistance provided through the Army Research Office grant DAAD19-02-1-0343, ARO Contract # W911NF-06-1-0216 and ARO Contract # Z-849901 and the assistance provided by Dr. A. Rajendren and Dr. M. Zikry and the support provided through DURIP grant DAAD19-01-1-0391 are gratefully acknowledged. Finally, the financial support provided by the University of South Carolina College of Engineering and Computing in support of the DURIP award is acknowledged.

References

1. Head H (1920) The sense of stability and balance in the Air. The Medical Problems of Flying, Oxford
2. Brown JL, Lechner M (1956) Acceleration and human performance; a survey of research. *J Aviat Med* 27(1):32–49
3. Duane T (1953) Preliminary Investigation into the Study of the Fundus Oculi of Human Subjects under Positive Acceleration. (Report No. NADC-MA-5303). Naval Air Development Center, Johnsville, PA
4. Stoll A (1956) Human tolerance to positive G as determined by the physiological End points. *J Aviat Med* 27(4):356–67
5. Eiband M (1959) Human tolerance to rapidly applied accelerations: a summary of the literature. Lewis Research Center, Cleveland, OH
6. Gurdjian ES, Lissner HR, Latimer FR, Haddad BF, Webster JE (1953) Quantitative determination of acceleration and intercranial pressure in experimental head injury. *Neurology* 3:417–423
7. Gurdjian ES, Roberts VL, Thomas LM (1964) Tolerance curves of acceleration and intercranial pressure and protective index in experimental head injury. *J Trauma* 600
8. Gurdjian ES, Hodgson VR, Hardy WG, Patrick LM, Lissner HR (1964) Evaluation of the Protective Characteristics of Helmets in Sports. *J Trauma* 4
9. Stech E, Payne P (1969) Dynamics of the human body (AD701383). Froster Engineering Development Corporation, Englewood CO
10. Verse J (1971) A review of the Severity Index. SAE Paper 710881. Proc. 15th Stapp Crash Conf. 771–795
11. Goldsmith W (1979) Some aspects of head and neck injury and protection. *Progress in biomechanics*. Sijthoff and Noordhoff, Alphen aan den Rijn, pp 333–377
12. Hutchinson J, Kaiser MJ, Lankarani HM (1998) The head injury criterion (HIC) functional[J]. *Appl Math Comput* 96:1–16
13. Marjoux D, Baumgartner D, Deck C, Willinger R (2008) Head injury prediction capability of the HIC, HIP, SIMon and ULP criteria. *Accid Anal Prev* 40:1135–1148
14. Department of Defense (1998) Crew Systems Crash Protection Handbook (JSSG-2010-7). Washington D.C.
15. US Army Aviation Systems Command (1989)
16. Eppinger et al. (1999) Development of Improved Injury Criteria for the Assessment of Advanced Automotive Restraint Systems-II. NHTSA, Nov
17. Eppinger et al. (2000) Supplement: Development of Improved Injury Criteria for the Assessment of Advanced Automotive Restraint Systems-II. NHTSA, March
18. Nurick GN, Shave GC (1995) The deformation and tearing of thin square plates subjected to impulsive loads-an experimental study. *Int J Impact Eng* 18(1):99–116

19. Jacob N, Chung KYS, Nurick GN, Bonorchis D, Desai SA, Tait D (2004) Scaling aspect of quadrangular plates subjected to localized blast loads-experiments and prediction. *Int J Impact Eng* 30:1179–1208
20. Nurick GN, Martin JB (1989) Deformation of thin plates subjected to impulsive loading-a review. Part II: experimental studies. *Int J Impact Eng* 8(2):171–86
21. Jacob N, Nurick GN, Langdon GS (2007) The effect of stand-off distance on the failure of fully clamped circular mild steel plate subjected to blast loads. *Eng Struct* 29:2723–2736
22. Fournay WL, Leiste U, Bonenberger R, Goodings D (2005) Mechanism of loading on plates due to detonation. *Fragblast Int J Blasting Fragm* 9(4):205–217
23. Fournay WL, Leiste U, Bonenberger R, Goodings D (2006) Explosive impulse on plates. *Fragblast Int J Blasting Fragm* 9(1):1–17
24. Fournay WL, Leiste U, Taylor L (2008) Pressures acting on targets subjected to explosive loading. *Fragblast Int. J. Blasting Fragm* 2: 167–187
25. Shcleyer GK, Lowak MJ, Poleyn MA, Langdon GS (2007) Experimental investigation of blast wall panels under shock pressure loading. *Int J Impact Eng* 34:1095–1118
26. Lawrence RW (1944) Mechanism of detonation in explosives. *J Gen Appl Geophys* 9:1–18
27. Hargather MJ, Settles GS (2007) Optical measurement and scaling of blasts from gram-range explosive charges. *Shock Waves* 17:215–223
28. Tiwari V, Sutton MA, McNeill SR, Xu SW, Deng XM (2009) Application of 3D image correlation for full-field transient plate deformation measurements during blast loading. *Int J Impact Eng* 36:862–874
29. Snyman IM (2010) Impulsive loading events and similarity scaling. *Eng Struct* 32:886–896
30. Fox DM, Huang X, Jung D, Fournay WL, Leiste U, Lee JS (2011) The Response of small scale rigid targets to shallow buried explosive detonations. *Int J Impact Eng* 38:882–891
31. Hopkinson B (1915) British Ordnance Board Minutes. 13565
32. Cranz C, der Ballistik L (1926) Textbook of ballistics. Springer Verlag, Berlin
33. Chabai AJ (1965) On Scaling dimensions of craters produced by buried explosives. *J Geophys Res* 70(20):5075–5098
34. Neuberger A, Peles S, Rittel D (2007) Scaling the response of circular plates subjected to large and close-range spherical explosions Part I: Air-blast loading. *Int J Impact Engineering* 34:859–873
35. Neuberger A, Peles S, Rittel D (2007) Scaling the response of circular plates subjected to large and close-range spherical explosions Part II: Buried charges. *Int J Impact Engineering* 34:874–882
36. Neuberger A, Peles S, Rittel D (2009) Springback of circular clamped armor steel plates subjected to spherical air-blast loading. *Int J Impact Engineering* 36:53–60
37. Bridgman PW (1949) Dimensional analysis. Yale University Press, New Haven, Conn
38. Jones N (1989) Structural impact. Cambridge University Press, New York
39. Gibbings JC (1982) Alogic of dimensional analysis. *J Phys A Math Gen* 15:1991–2002
40. Gibbings JC (1986) The systematic experiments. Cambridge University Press, Cambridge
41. Genson K (2006) Vehicle shaping for mine blast damage reduction. MSc thesis, University of Maryland, USA
42. Benedetti R (2008) Mitigation of explosive blast effects on vehicle floorboard. MSc thesis, University of Maryland, USA
43. Fournay WL, Leiste HU, Hauck A, Jung D (2010) Distribution of Specific Impulse on Vehicles Subjected to IED's Proceedings of SEM Fall Conference, IMPLAST 2010 held in Providence RI